

Improving the performance of PERC silicon solar cells by optimizing the surface inverted pyramid structure on large-area mono-crystalline silicon wafers



Danni Zhang^{a,b}, Longjie Wang^{a,b}, Rui Jia^{a,b,*}, Ke Tao^{a,b,**}, Shuai Jiang^a, Huayun Ge^{a,b}, Bolong Wang^{a,b}, Zhibo Gao^a, Xinpu Li^c, Minghui Li^a, Zhi Jin^{a,b}

^a Institute of Microelectronics of Chinese Academy of Sciences, Beijing, 100029, China

^b University of Chinese Academy of Sciences, Beijing, 100029, China

^c Hanwha-Qcells, Jiangsu, 226200, China

ARTICLE INFO

Keywords:

Texture
Nanoparticles
PERC Solar cells
Inverted pyramids
Efficiency
Cu metal assisted chemical etching (Cu-MACE)

ABSTRACT

Optimizing the surface texture of silicon wafer to improve the light trapping performance and effective carrier lifetime of silicon surface is an efficient and low-cost way to enhance the energy conversion efficiency of mono-crystalline silicon PERC solar cells. In this paper, a simple method was adopted to prepare inverted pyramids with different sizes by varying the ρ value ($\rho = [\text{HF}] / ([\text{HF}] + [\text{H}_2\text{O}_2])$) of Cu metal assisted chemical etching (Cu-MACE) etching solution. The chemical mechanism of formation, etching rate, surface reflectivity, and effective minority carrier lifetime mapping of different silicon surface structures were systematically investigated. Moreover, the solar energy absorption rate of these different surface structures were studied by the finite difference time domain (FDTD) method. The results show that when the ρ value was between 25% and 90%, the etching rate of Cu nanoparticles increases with increasing ρ value. The final results reveal that the surface reflectivity, effective minority carrier lifetime and the light absorption were optimal when $\rho \sim 75\%$, and the uniformity of corresponding inverted pyramid texture is the best. By utilizing the best inverted pyramid texture, the highest efficiency is 22.69%, corresponding V_{oc} is 680.42 mV, J_{sc} is 41.20 mA/cm², and FF is 80.94% on the 156.75 × 156.75 mm² for large area mono-crystalline silicon PERC solar cell.

1. Introduction

In recent years, passivated emitter and rear cell (PERC) has become the mainstream technology of mono-crystalline silicon solar cell due to its high conversion efficiency and low process cost [1,2]. Improving the solar cell efficiency and reducing the production cost are vital to the development of solar cell industry. Texturing process is the crucial step to enhance the light absorption of silicon wafer in all the processes of solar cell [1–3]. Therefore, many researchers want to optimize the texture structures of silicon surface through simple changes to achieve the purpose of increasing the conversion efficiency of solar cell.

Generally, alkaline etching (KOH) based on anisotropic etching is utilized to texture mono-crystalline silicon wafers in almost all factories. The alkaline etching forms randomly distributed pyramid structures on the silicon substrate [1,2]. However, the efficiency of PERC cells with

pyramid texture has gradually entered a bottleneck period [4,5]. One of the main reason is that the light trapping property of the pyramid structure limits the device performance [5]. Therefore, it is significant to research the preparation of inverted pyramid structures on the silicon surface to improve the performance of mono-crystalline silicon PERC solar cell.

Many studies share that most of incident light is reflected three or more times on the surface of inverted pyramid structures, while most of incident light is reflected only once or twice times on pyramid structures [6]. Therefore, the inverted pyramid structure can increase the reflection path length of the incident light, thus it enhance the light trapping properties of the surface. Moreover, the inverted pyramid structure can greatly reduce serious surface recombination due to its large and open features [7–9]. More importantly, inverted pyramid texture with the trait of concave structure is very suitable for coating and filling, such as

* Corresponding author. Institute of Microelectronics of Chinese Academy of Sciences, Beijing, 100029, China.

** Corresponding author. Institute of Microelectronics of Chinese Academy of Sciences, Beijing, 100029, China.

E-mail addresses: imesolar@126.com (R. Jia), taoke@ime.ac.cn (K. Tao).

SiN_x layers and metal electrodes in solar cells [10–12]. As a consequence, the inverted pyramid has a great potential to improve the performance of solar cells. Until now, many different methods have been applied to fabricate inverted pyramid texture on the surface of mono-crystalline silicon wafer, mainly including: reactive ion etching (RIE) method [13], lithography technology [14], laser technique [15], and metal assisted chemical etching (MACE) method [16,17]. Among the above methods, the MACE method is widely adopted in large-scale industrial production due to its excellent economic benefits and compatibility with existing production lines. Other methods are not suitable for industrial production on account of expensive facilities and low output. Ag and Cu are the two most commonly used metal catalysts for MACE method [18–22]. Importantly, Cu MACE take advantages over Ag by its relatively low cost and reliability [6,7,17,23]. Interestingly, Cu MACE can etch different types of inverted pyramid structures on the surface of silicon wafers [24]. Although a great deal of substantial work has been devoted to study the light trapping characteristics of inverted pyramids with different structures [10–14,20], the effect of disparate inverted pyramids on the performance of large-area mono-crystalline silicon PERC solar cell is rarely studied.

In this paper, inverted pyramids with different shapes were prepared on the surface of mono-crystalline silicon wafer through changing the ρ value ($\rho = [\text{HF}] / ([\text{HF}] + [\text{H}_2\text{O}_2])$) of Cu MACE etching solution. On this basis, the influence of different inverted pyramid processes on etching rate, surface reflectivity, and effective minority carrier lifetime was systematically analyzed. At the same time, the chemical mechanism of the formation of inverted pyramids with different morphologies was discussed in detail. Furthermore, we utilized FDTD method to investigate the solar energy absorption of these different textures. Finally, by adopting the optimized inverted pyramid texture, the highest energy conversion rate is 22.69%, open circuit voltage (V_{oc}) is 680.42 mV, short circuit current (J_{sc}) is 41.20 mA/cm², and fill factor (FF) is 80.94% on mono-crystalline silicon PERC solar cell with large area of 156.75 × 156.75 mm². This indicates that the Cu-MACE has a great application prospect in the large-scale industrial production of PERC solar cells.

2. Experimental section

156.75mm × 156.75 mm P-type (100-oriented) diamond-wire-sawn (DWS) mono-crystalline silicon wafers (resistivity, 1–3 Ω•cm) with a thickness of 200 ± 10 μm were used in this work. Firstly, all mono-crystalline silicon wafers were immersed in 25 wt% KOH solution at 80 °C to remove the saw damage layer, Fig. 1 shows the plan view SEM images of mono-crystalline silicon wafer before and after removing the saw damage layer. Secondly, the mono-crystalline silicon wafers were etched in mixed aqueous solutions of $\text{Cu}(\text{NO}_3)_2/\text{HF}/\text{H}_2\text{O}_2$ solution for 15 min to form nanostructures at 50 °C.

In order to investigate the influence of surface morphology of mono-crystalline silicon on device performance, the surface morphology was modulated by changing ρ value, and other conditions were kept fixed. ρ value is defined as $\rho = [\text{HF}] / ([\text{HF}] + [\text{H}_2\text{O}_2])$. Table 1 lists the corresponding experimental conditions. For the simplicity of expression, the ρ values are 25%, 50%, 75%, and 90%, respectively. Thirdly, the wafers with nanostructures were post-processed in two steps: (i) immersed the wafers in a HF/HNO₃ mixture solution to expand the nanostructure at room temperature for 1 min. (ii) dipped them into the diluted KOH solution at room temperature for 1 min to smooth the surface of inverted pyramids. Finally, these mono-crystalline silicon wafers were treated in concentrated nitric acid (HNO₃) at room temperature for 5 min to remove the residual copper nanoparticles. All the mono-crystalline silicon wafers were rinsed at least 1 min by deionized water after each step.

These samples with different types of textures underwent the following standard PERC solar cell manufacturing process (shown in Fig. 2): (i) POCl_3 diffusion to form PN junction on the front surface of the wafer. (ii) Laser doping for selective emitter. (iii) Front side etching for the target of removing phosphorosilicate glass (PSG), and rear side polishing. (iv) The front of wafer was covered with SiO_2 by thermal oxidation. (v) Al_2O_3 film were deposited on the rear surface of wafer by atomic layer deposition (ALD). (vi) Deposition of SiN_x coating on front surface and rear surface by plasma enhanced chemical vapor deposition (PECVD) system. (vii) The rear passivation layer was locally ablated by laser. (viii) screen printing and co-firing to form metal electrodes and metal contacts. The device diagram of mono-crystalline silicon PERC solar cell with inverted pyramid structures is exhibited in Fig. 3.

The surface morphology of the mono-crystalline silicon wafer was measured by scanning electron microscopy (SEM, Hitachi, S4800, Chiyoda-ku, Japan). The surface reflectivity of silicon wafers, internal quantum efficiency (IQE) and external quantum efficiency (EQE) of solar cells were investigated by the solar cell measurement system (Sofn, 7-SCSpecII, China). The effective minority carrier lifetime mapping of passivated samples were characterized by Semilab PV 2000. The electrical performance of solar cells were measured by a current-voltage (I-V) measurement system under standard testing conditions (AM1.5G, 1000W/m², 25 ± 2 °C.). Three dimensional finite difference

Table 1
Different etching conditions for Cu MACE.

Sample	$\text{Cu}(\text{NO}_3)_2$ (mol/L)	HF (mol/L)	H_2O_2 (mol/L)	Temperature (°C)	Etching time (min)
$\rho=25\%$	0.025	0.5	1.5	50	15
$\rho=50\%$	0.025	1.5	1.5	50	15
$\rho=75\%$	0.025	4.5	1.5	50	15
$\rho=90\%$	0.025	13.5	1.5	50	15

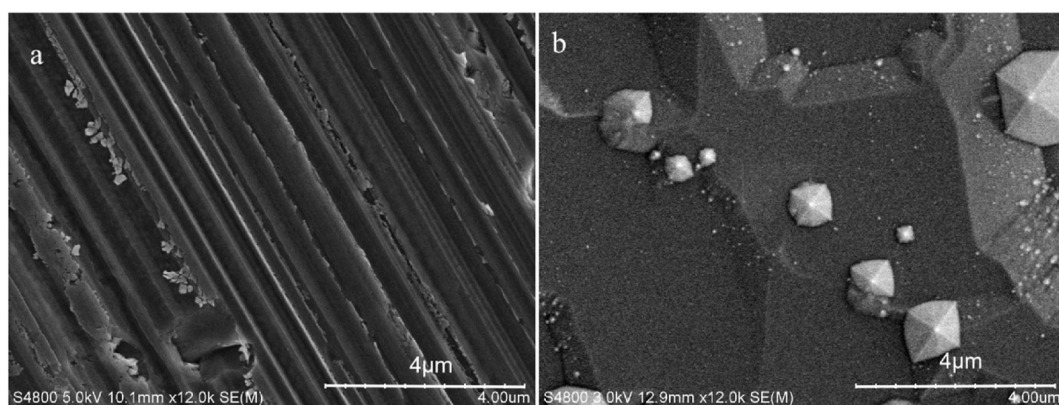


Fig. 1. Plan view SEM images of mono-crystalline silicon wafer before and after removing the saw damage layer: (a) diamond-wire-sawn mono-crystalline silicon wafer, (b) saw damage layer removed.

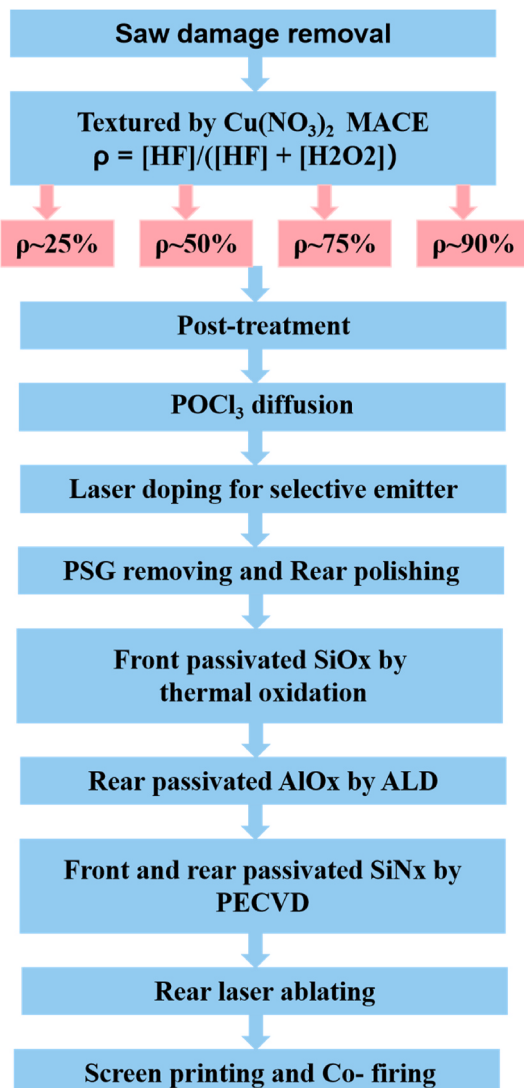


Fig. 2. Fabrication process for mono-crystalline silicon PERC solar cells.

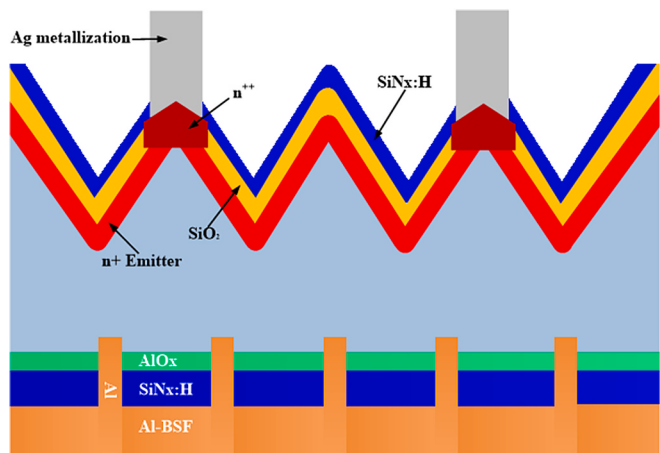


Fig. 3. The device diagram of mono-crystalline silicon PERC solar cell with inverted pyramid structures.

time domain (FDTD) simulations were performed to analyze the electromagnetic field distribution and optical absorption properties of different nanostructures on the silicon substrates.

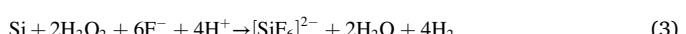
3. Results and discussion

Fig. 4a1~d2 compare the surface morphology of mono-crystalline silicon wafers at etch compositions ρ value varying from 25% to 90%. It can be clearly seen that the surfaces of all sample surfaces were densely distributed with nanostructures, the texture morphology and structure size were strongly correlated with the ρ value. Fig. 4a1 and a2 show that low ρ value contributes to the sporadic shallow sponge-like structures on the surface of mono-crystalline silicon wafers. When $\rho \sim 50\%$ was adopted, more inverted pyramid structures were observed on the surface of mono-crystalline silicon wafer and their sizes become larger in average. With regarding to $\rho \sim 75\%$, the surface of mono-crystalline silicon wafers was covered by randomly distributed inverted pyramid structures with lateral mean size of 1.4–2.4 μm , shown in Fig. 4c1 and c2, and a little rough side walls appeared on inverted pyramids. These results are likely related to the anisotropic etching characteristics of copper particles. When $\rho \sim 90\%$, the side walls of inverted pyramids (Fig. 4d1 and d2) were corroded, resulting in merging and overlapping of some inverted pyramids to form gully structures and semicircle structures. In addition, some triangles and small inverted pyramid structures were formed on the side wall of the gully structure.

As the final different structure morphologies can be greatly affected by the variation of ρ values with the other conditions kept fixed. Therefore, it is necessary to propose a reasonable dynamic etching model to explain the following two issues: (1) How does the ρ value influence the surface morphology on the mono-crystalline silicon wafer? (2) How does the ρ value affect the deposition behavior of Cu nanoparticles on the surface of mono-crystalline silicon wafer? In order to figure out the above issues, the dynamic etching mechanism under the Cu MACE process should be explained.

Fig. 5 illustrates the formation of the textures with different sizes and surface morphologies fabricated under various ρ values. When a low ρ value was used, the concentration of HF was very low, so the oxide layer cannot be rapidly removed in the absence of HF in the solution. The Cu nanoparticles depositing on the silicon surface were quickly consumed and disappeared. Therefore, the shallow and small structures covered on the silicon surface due to the short lifetime of Cu nanoparticles. When a medium ρ value was adopted, the inverted pyramid structures formed step by step. The chemical reactions achieved dynamic equilibrium gradually in the etching solution. The anisotropic etching occurred on the surface of silicon wafer. The uniform inverted pyramids were achieved with the appropriate proportion of HF in the etching solution. A high ρ value means a high concentration of HF in the solution, which leads to rapid etching of silicon and rapid consumption of H₂O₂ in the etching solution, resulting in extremely uneven texture structures. After H₂O₂ depletion, Cu nanoparticles deposited on the surface of the silicon wafer, but could not be dissolved. Silicon dioxide will be directly dissolved by surplus HF, which allows the silicon substrate to release more reductive hydrogen gas. This H₂ induced more copper ions to reduce and deposit on the surface of silicon wafer. The size of Cu nanoparticles increased with the deposition of Cu nanoparticles, and a brown-red copper film was gradually formed on the surface of the silicon wafer. The copper film were then removed by concentrated nitric acid. Eq. (1) ~ (5) express the chemical reaction in the etchant solution [19,25,26].

Anodic reaction:



Cathodic reaction:



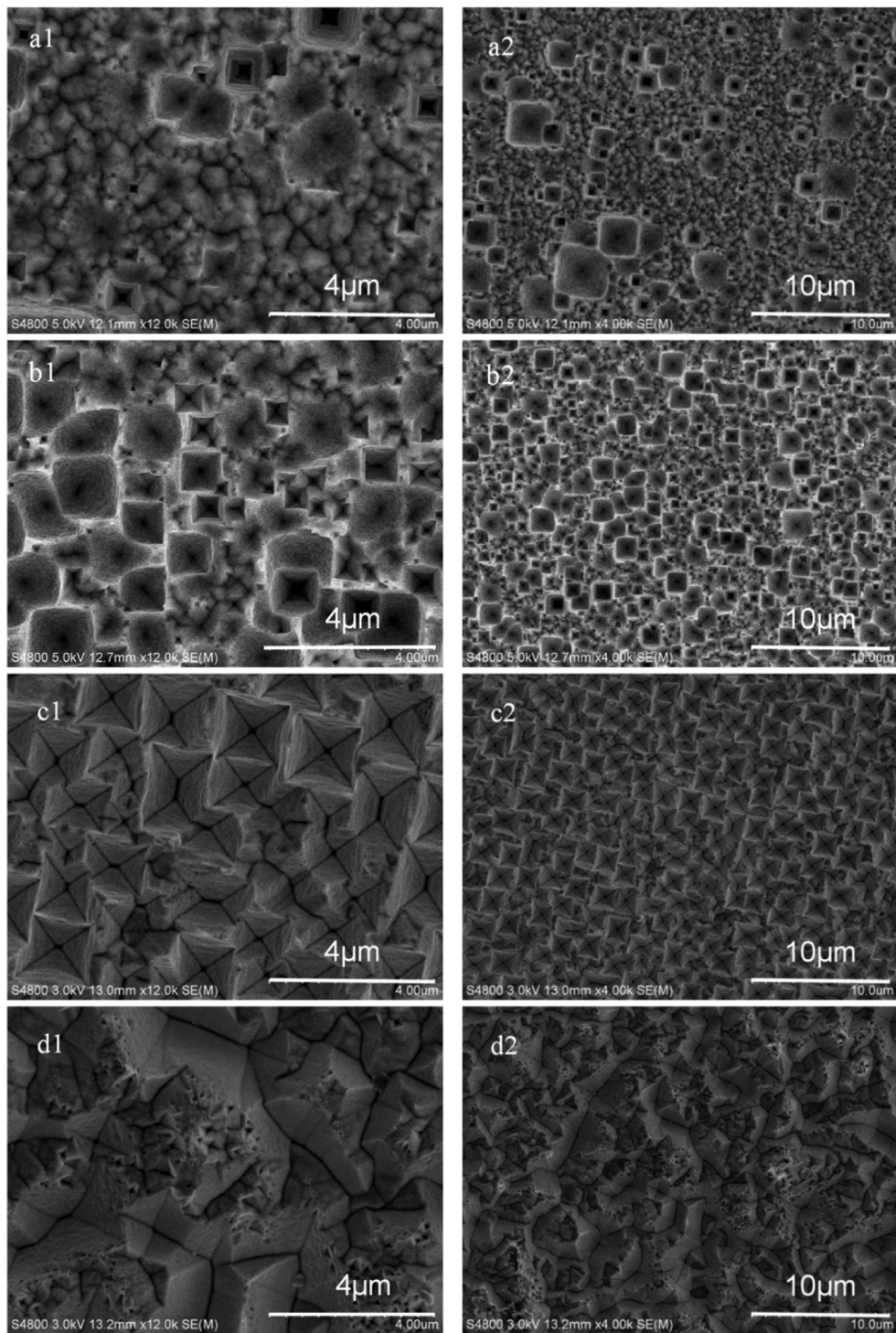


Fig. 4. Plan view SEM images of the mono-crystalline silicon wafers fabricated by different ρ values: (a1,a2) $\rho \sim 25\%$; (b1,b2) $\rho \sim 50\%$; (c1,c2) $\rho \sim 75\%$; (d1, d2) $\rho \sim 90\%$.

Fig. 6a ~ d show the cross-sectional SEM images of the silicon nanostructures. It can be clearly seen that the depth of the nanostructure increases with the rise of ρ value, which indicates that the etching rate accelerates as the increase of ρ value.

In order to characterize the etching rate of silicon substrate at etching process, the average etching rate R_{av} is introduced as Eq. (6) [7].

$$R_{av} = \frac{\Delta m}{2\rho_{si}St} \quad (6)$$

Where Δm is the total mass loss of mono-crystalline silicon wafer after etching, ρ_{si} is the Si density ($\rho_{si} = 2.33 \text{ g/cm}^3$), S is the surface area of the sample ($S = 156.75 \times 156.75 \text{ mm}^2$), and t is the etching time ($t = 15 \text{ min}$). **Fig. 7** exhibits the relationship between weight loss, etching rate and ρ value of different samples. The results shown in **Fig. 7** further proved that the etching rate increase with the rise of ρ value.

In order to explain the reason why the etching rate varies with the change of ρ value, the Nernst equation can be introduced to characterize the etching process at equilibrium state. The Nernst equation is shown in

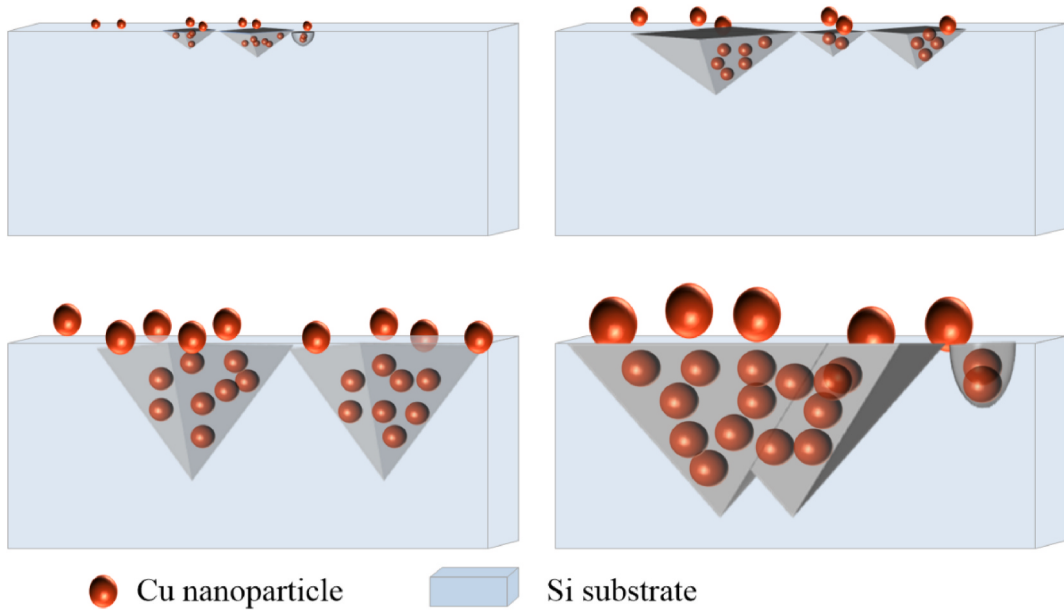


Fig. 5. Schematic diagram of the deposition behavior of Cu nanoparticles under different ρ values: (a) $\rho \sim 25\%$; (b) $\rho \sim 50\%$; (c) $\rho \sim 75\%$; (d) $\rho \sim 90\%$.

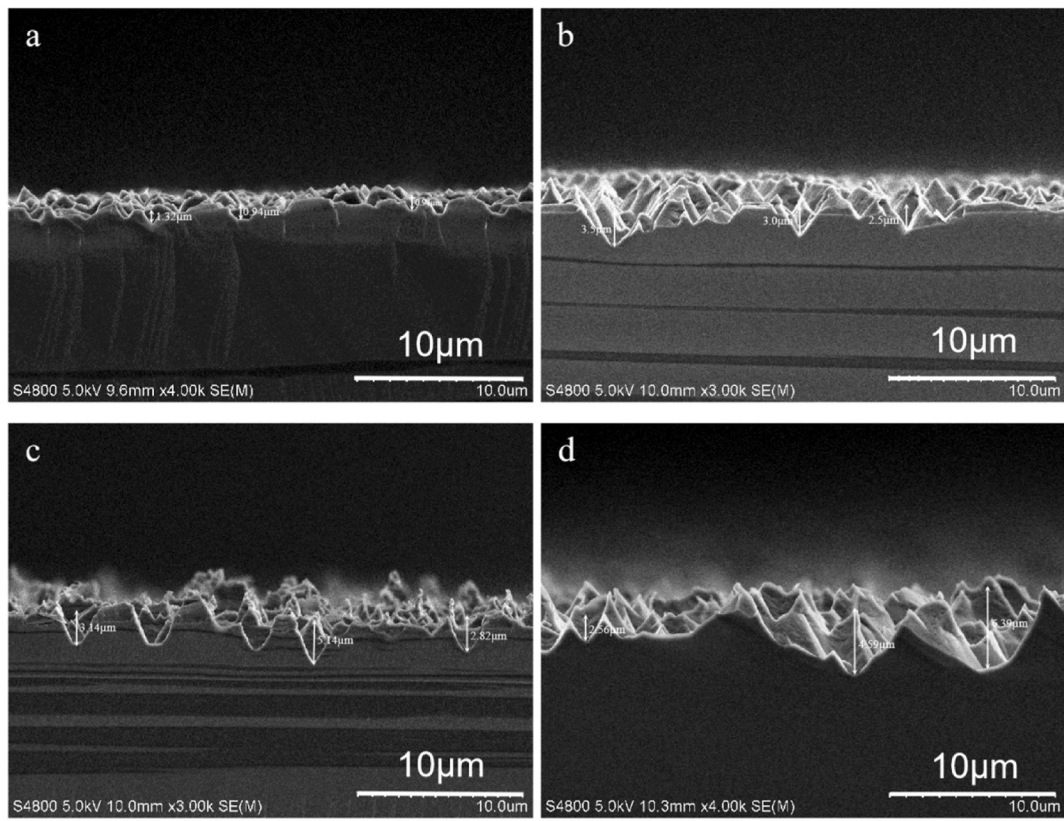


Fig. 6. SEM images cross section of mono-crystalline silicon wafers fabricated by different ρ values: (a) $\rho \sim 25\%$; (b) $\rho \sim 50\%$; (c) $\rho \sim 75\%$; (d) $\rho \sim 90\%$.

Eq. (7) [26].

$$\Delta E = \Delta E_0 + \frac{RT}{2F} \ln \frac{[H_2O_2]^2 [F^-]^6 [H^+]^4}{[SiF_6^{2-}]} \quad (7)$$

In which ΔE is equilibrium potential, ΔE_0 is the equilibrium potential in standard condition, R is the ideal-gas constant $8.314 \text{ J k}^{-1}\text{mol}^{-1}$, T is the absolute temperature, $[H_2O_2]$, $[F^-]$, $[H^+]$ and $[SiF_6^{2-}]$ are the molar concentration of the corresponding components in the etchant solution,

respectively. It can be seen from the right-hand side of Eq. (7), ΔE is proportional to the square of $[H_2O_2]$ and the sixth power of $[F^-]$, indicating that the influence of $[F^-]$ on the ΔE is greater than that of $[H_2O_2]$. Therefore, with the change of ρ ($[HF]/([HF] + [H_2O_2])$) values from 25% to 90%, the ΔE value tends to increase due to the increase of $[F^-]$, resulting in the gradual increase of etching rate. As demonstrated in Fig. 7, when the ρ value is small, the etching rate slowly increases as the increase of ρ value, while when ρ value is large, the etching rate rapidly

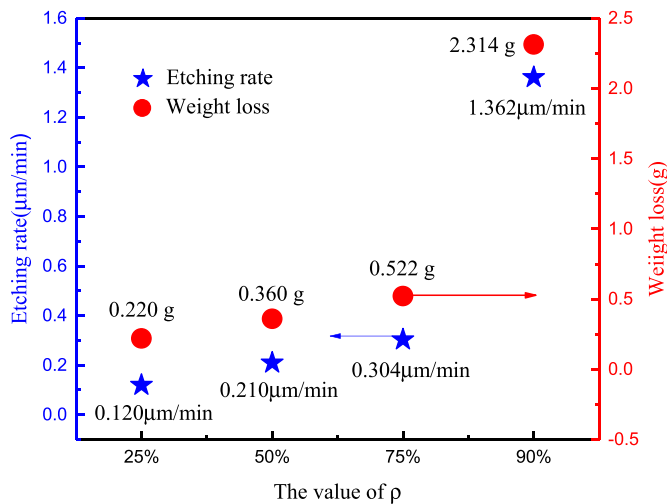


Fig. 7. The etching rate and weight loss of mono-crystalline silicon wafer during etching process in etchant solutions with different ρ values.

increases with the ρ value increasing. The above results explain the reasons for surface morphology influenced by ρ values, and deposition behavior of Cu nanoparticles at different ρ values.

In order to assess the light capture capability of different surface structures, the weighted average reflectivity without and with SiNx layer of four different surface structures have been investigated. The reflectivity spectra of the samples without and with SiNx layer in wavelength range from 300 nm to 1100 nm are presented in Fig. 6a and b, respectively. And the weighted average reflectivity R_w are listed in Table 2, which calculated by Eq. (8) [10].

$$R_w = \frac{\int_{300}^{1100} R(\lambda)N(\lambda)d\lambda}{\int_{300}^{1100} N(\lambda)d\lambda} \quad (8)$$

where $R(\lambda)$ is the total reflectance, $N(\lambda)$ is the solar flux under AM 1.5 standard condition.

The $\rho \sim 75\%$ obtained the lowest average reflectance of 5.45%, while the $\rho \sim 50\%$ sample show a higher but still suitable anti-reflection properties, ascribing to the powerful forward scattering in Mie scattering theory, which makes the inverted pyramid structures enhanced the light harvest capability [27]. Furthermore, inverted pyramid structures bounced the incident light multiple times to reduce the amount of light escaping back into the air. For $\rho \sim 90\%$, since a lot of gully structures and tiny triangles attached to its side walls present on the silicon surface, the light capture performance become weak with a high reflectivity of 14.78%. In addition, the sizes of the overlapping and gully structure are larger than the wavelength of the target light, resulting in poor light trapping [26]. The weight average reflectivity for $\rho \sim 25\%$ is 11.07%, because of the shallow and small structures on the silicon surface limits the propagation length of the incident light in these structures. After depositing SiNx layer, the reflectivity of all samples

Table 2

The weight average reflectivity of four different surface structures in the range of 300–1100 nm.

Sample	Surface average reflectivity after texturing process(%)	Surface average reflectivity after coating SiNx layer(%)
$\rho \sim 25\%$	11.07	4.01
$\rho \sim 50\%$	7.44	2.76
$\rho \sim 75\%$	5.45	2.09
$\rho \sim 90\%$	14.78	5.44
Upright pyramid	13.02	4.12
Saw damage removed	40.63	—

significantly reduced due to the graded refractive index [28], as shown in Fig. 8b. Therefore, the optical performance of silicon surface can be effectively controlled by changing the ρ value (see Fig. 8).

In order to investigate the light absorption mechanism of different nanostructures on the surface of silicon wafers, the three dimensional finite difference time domain (FDTD) analysis was employed to visually analyze the electromagnetic field distribution and optical absorption. Fig. 9 shows the schematic model of different nanostructures. The rectangle of the solid red line is the actual simulation area. In the design, the x-axis and y-axis directions were set as the Periodic boundary conditions, and the smaller unit cells were utilized to simulate a wider characteristic array. While, the Perfectly Matched Layers (PML) were adopted in the z-axis direction to avoid parasitic reflection and absorption [29]. A plane wave source with the wavelength of 631.75 nm was utilized to calculate electromagnetic field distribution because it is close to the peak irradiance of the solar spectrum [29]. The light source was illuminated from the top and along the negative direction of the z-axis direction. The simulation parameters of the models were achieved according to the average values of the SEM images shown in Figs. 4 and 6.

As shown in Fig. 10a and b, the highest electric field intensities are confined to the inverted pyramid structures and there are also strong electric field outside the structures. Besides, the high electric field is not observed in the small inverted pyramid structures and shallow pits. What's more, there is almost no electric field outside these structures. These results demonstrate that the absorption capacity of these structures for incident photons is very poor. For uniform inverted pyramid

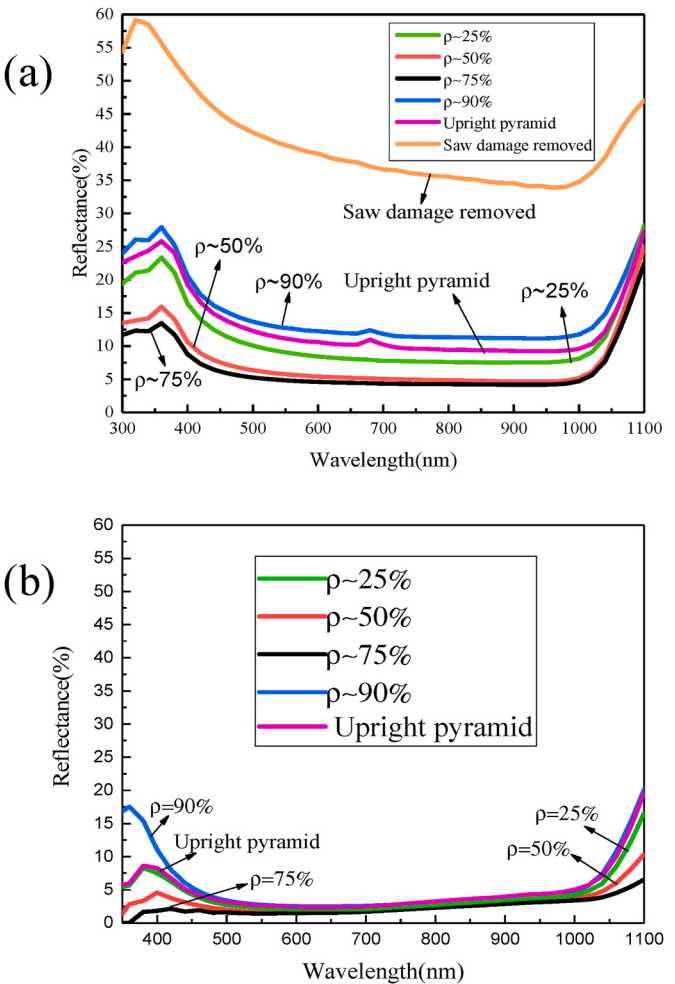


Fig. 8. (a) the reflectivity curves of different surface morphologies; (b) the reflectivity curves of different surface morphologies after coating SiNx layer.

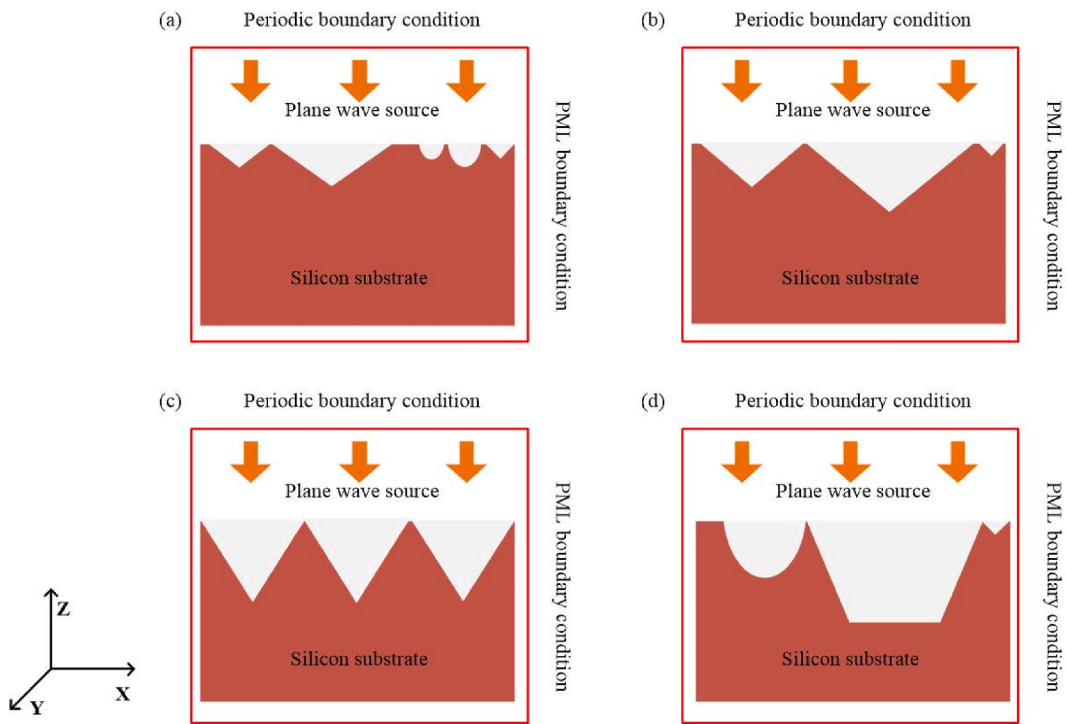


Fig. 9. Cross section of the unit cell used in the simulations, including the overall unit cell boundaries.

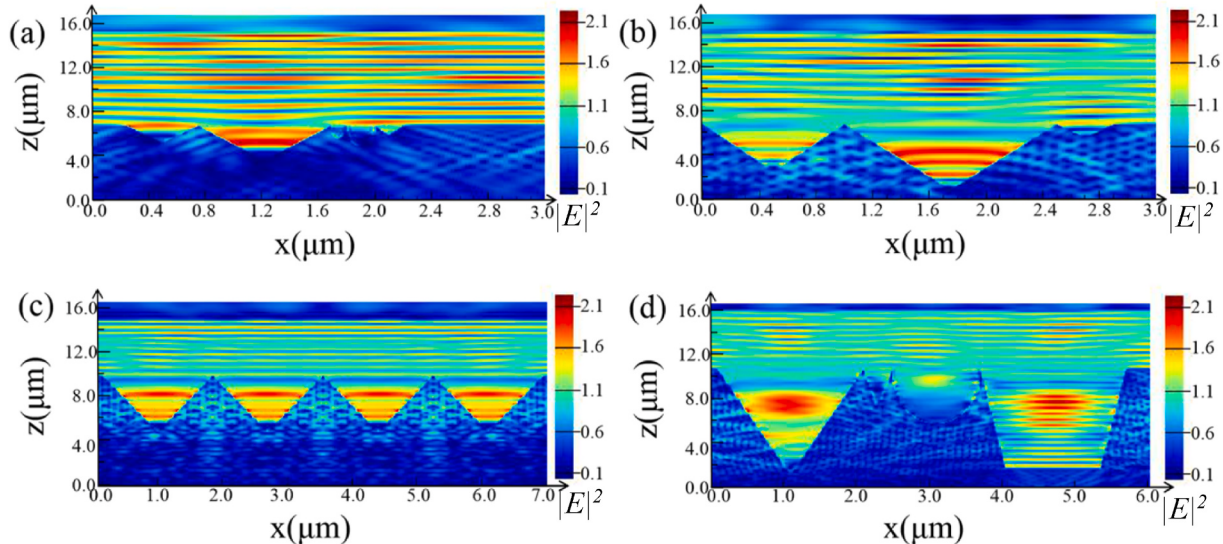


Fig. 10. The simulation results of the cross-sectional electric field $|E|^2$ distribution of different surface structures. (a) shallow pits and tiny inverted pyramid structures; (b) small and shallow inverted pyramid structures; (c) uniform inverted pyramid structures; (d) overlapping structure, large inverted pyramid and deep holes.

structures in Fig. 10c, the highest electric field distribute inside the inverted pyramid structures. The high electric field are caused by the increase of optical absorption and electron-hole pairs due to the photo-coupling [29]. Therefore, the results indicated that the uniform inverted pyramid structures can significantly increase the absorption of incoming photon energy. The high electric field in Fig. 10d is restricted in the middle of large inverted pyramid and overlapping structure, but doesn't cover the whole region of structures. And the high energy field is completely absent in the deep pore and shallow pit structures. Which indicated that the ability of these structures absorbing incident photon energy is thin. In a word, the absorption of incident photon energy heavily depends on the geometric parameters of the surface structure.

And the uniform inverted pyramid structures possess the superior photon harvesting capability.

After double side phosphorous diffusion, double side PSG removal, and double side SiNx layer deposition, the effective minority carrier lifetime (τ_{eff}) of the samples were tested by Semilab PV-2000. Although the size of the sample is $156.75 \times 156.75 \text{ mm}^2$, but the actual testing area is $140 \times 140 \text{ mm}^2$ [30]. Fig. 11 and Table 3 show the effective minority carrier lifetime mapping and corresponding statistic data, respectively.

Based on the test results in Fig. 11, the distribution of minority lifetime in $\rho \sim 75\%$ is more uniform than others. And the mapping of $\rho \sim 25\%$ and $\rho \sim 90\%$ have more regions with low minority lifetime than

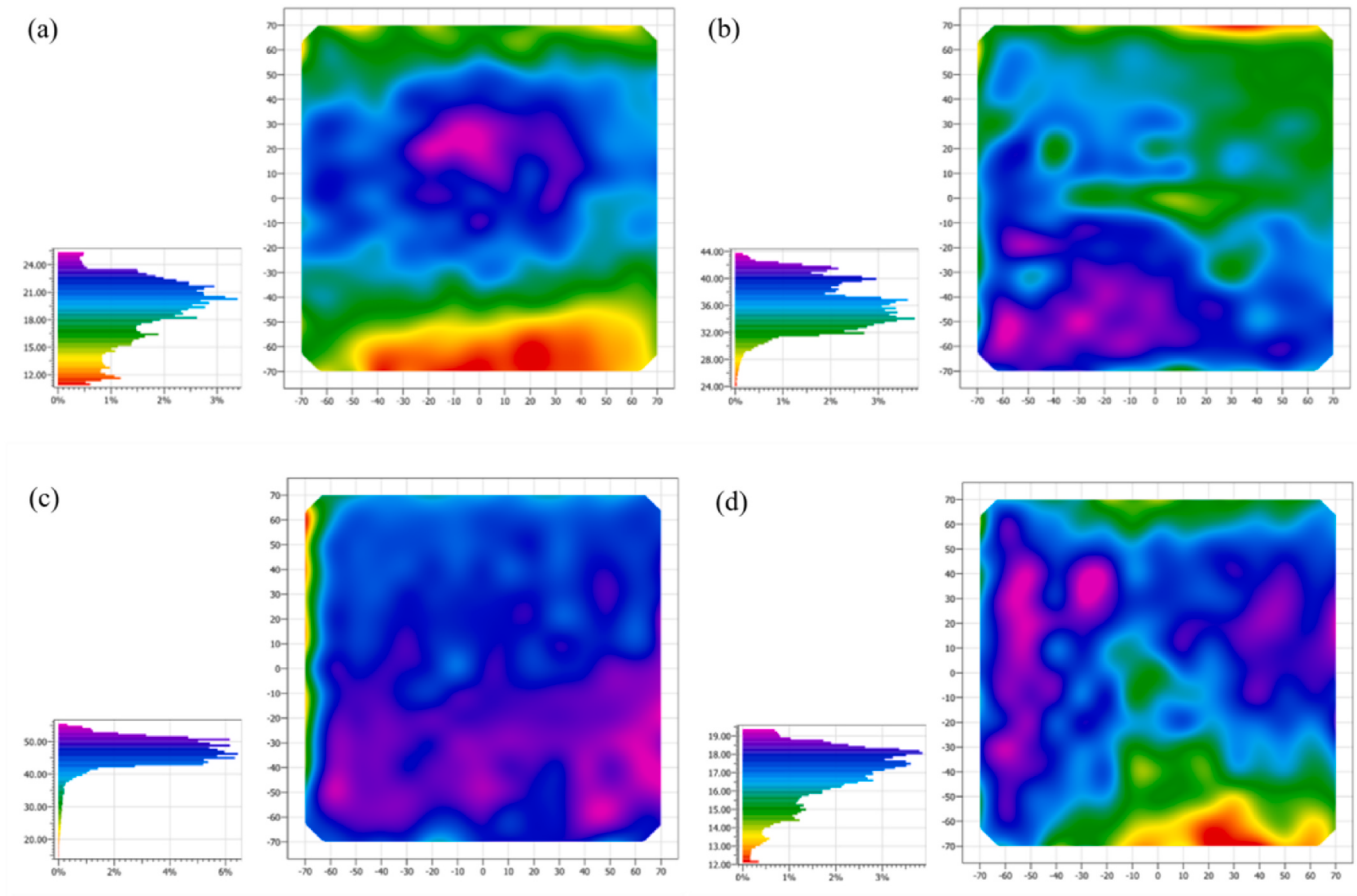


Fig. 11. The effective minority carrier lifetime mapping of samples. (a) $\rho \sim 25\%$; (b) $\rho \sim 50\%$; (c) $\rho \sim 75\%$; (d) $\rho \sim 90\%$.

Table 3

Effective minority carrier lifetime parameters of samples.

Sample	Average (μs)	Minimum(μs)	Maximum(μs)	S_{ave} (cm/s)
$\rho \sim 25\%$	18.63	10.94	25.49	505.53
$\rho \sim 50\%$	36.07	24.17	43.94	503.53
$\rho \sim 75\%$	46.40	14.86	55.83	252.44
$\rho \sim 90\%$	16.78	12.15	19.43	541.96

that of $\rho \sim 50\%$ and $\rho \sim 75\%$. There are three main factors function together to reduce the minority lifetime of $\rho \sim 25\%$ and $\rho \sim 90\%$ group. First, the small triangle structures increased the local specific surface area of $\rho \sim 25\%$ group and $\rho \sim 90\%$ group, which enhanced phosphorus doping [31], thus augmented the Auger recombination of these samples [33]; Second, in $\rho \sim 90\%$ group, the triangles and small inverted pyramids on the side walls of large structures are regarded as recombination centers, which caused serious surface recombination; Third, for the same reason, the samples of $\rho \sim 25\%$ group and $\rho \sim 90\%$ group suffer a poor surface passivation.

Table 3 lists the effective minority carrier lifetime and recombination velocity of the samples. In which, S_{ave} is the average surface recombination velocity of minority carrier. It's obvious that the average lifetime of $\rho \sim 75\%$ group is much higher than that of others. Furthermore, the samples of $\rho \sim 75\%$ show much lower surface recombination velocity, which indicates that $\rho \sim 75\%$ group possess better SiNx passivation quality.

Fig. 12 shows the internal quantum efficiency (IQE) and external quantum efficiency (EQE) spectra of PERC solar cells with different surface conditions. It indicates that the PERC solar cell of $\rho \sim 75\%$ group exhibits a better IQE and EQE than that of others, especially in blue

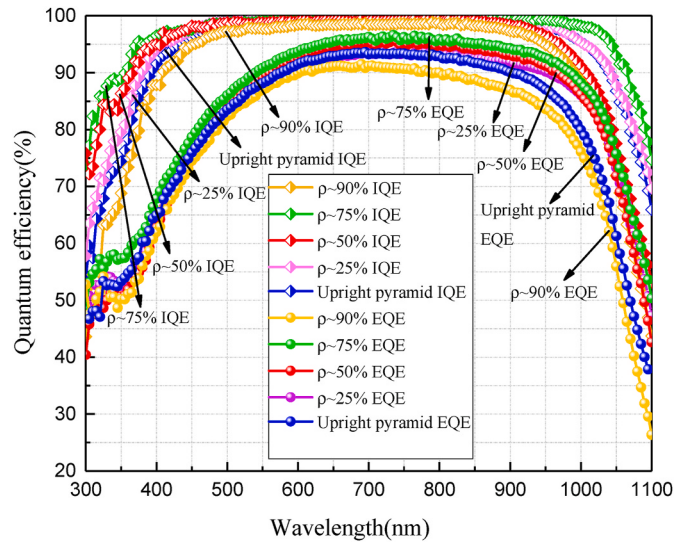


Fig. 12. The quantum efficiency (IQE and EQE) as a function of wavelength 300–1100 nm of mono-crystalline silicon PERC solar cell fabricated by different ρ values.

response and infrared response. At the blue response area, two factors may contribute to enhancing the blue response in $\rho \sim 75\%$ group: (1) surface recombination due to local high surface area of $\rho \sim 25\%$ group and $\rho \sim 90\%$ group; and (2) Auger recombination due to local heavy emitter doping in $\rho \sim 25\%$ group and $\rho \sim 90\%$ group, which is caused by in-diffusion of phosphorous from the tiny triangular nanostructures with

high surface area [31]. Uniform and shallower inverted pyramid not only reduces the problems of surface recombination and Auger recombination, but also is related to more uniform PN junction depletion region and high passivation performance of SiNx coating, thus improving the blue response of $\rho \sim 75\%$ group. In the infrared region, the IQE and EQE of $\rho \sim 75\%$ group is higher than that of others. This can be attributed to the uniform inverted pyramid structures inducing light absorption enhancement in the infrared region and a higher quality back surface field passivation.

Fig. 13 and **Table 4** show the electrical performance of the solar cells fabricated by different ρ values. It can be seen obviously that the photoelectric conversion efficiency of $\rho \sim 75\%$ group is highest, for 22.69%, which is 0.66%, 0.27% and 1.28% absolute higher than that of $\rho \sim 25\%$, $\rho \sim 50\%$ and $\rho \sim 90\%$ group, respectively.

In order to systematically evaluate the light trapping performance of the PERC solar cells with different surface structures, the calculated and measured short-circuit current (J_{sc}) of all samples are compared in **Table 4**. The J_{sc} for AM 1.5G solar illumination is calculated according to the equation as follows [32]:

$$J_{sc} = q \int_{\lambda_1}^{\lambda_2} EQE(\lambda) \Phi_{ph,\lambda}^{AM1.5} d\lambda \quad (9)$$

Where q is the elementary charge, $[\lambda_1, \lambda_2]$ is the wavelength of incident light, $\Phi_{ph,\lambda}^{AM1.5}$ is the spectral photon flux, and $EQE(\lambda)$ is obtained from **Fig. 12**. The calculated results of each group are shown in **Table 4**. And the wavelength range for calculating J_{sc} is controlled in 300–1100 nm.

From **Table 4**, it can be seen that the variation trend of J_{sc} calculated by EQE is consistent with that of J_{sc} measured by IV curve (as shown in **Fig. 13**). J_{sc} has its maximum (41.20 mA/cm^2) in $\rho \sim 75\%$ based cell, which possesses the lowest reflective and the best performance of light trapping. Correspondingly, $\rho \sim 75\%$ based cell obtained the maximum open-circuit voltage (V_{oc}) of 680.42 mV. There are two possible reasons for this result. One is that the uniform inverted pyramid structure reduces surface recombination and Auger recombination. The other is that the uniform inverted pyramid structures improve the passivation quality of SiNx coating. Therefore, the excellent light trapping and high performance mono-crystalline silicon PERC solar cell can be implemented by modified the surface texture.

In addition, the calculated J_{sc} are smaller than the measured J_{sc} from the IV curve in **Table 4**. There are three possible factors for this phenomenon. First, the AM 1.5 spectrum used in EQE system is standard data but in case of solar simulator that is simulated by a xenon lamp. Second, the illumination area in the EQE system is smaller than that of the solar simulator, so the generating area of charge carrier in EQE system is smaller, while the area in the IV system is larger. Third, the measurement errors and calculation errors also lead to the difference between the calculated J_{sc} and the measured J_{sc} .

4. Conclusion

In conclusion, various texture structures have been fabricated on mono-crystalline silicon wafers by changing ρ value of Cu MACE etching solution. The effects of different ρ values on the nanostructure and chemical mechanism were systematically investigated. Low ρ value leads to the tiny shallow nanoholes which has poor light trapping ability, while high ρ value results in overlapping structures and deep pores that deteriorate solar cell performance. $\rho \sim 75\%$ group obtained the uniform inverted pyramid structures on the surface of mono-crystalline silicon wafer. The results of reflectivity and FDTD simulation show that uniform inverted pyramid structure has significant advantages in optical absorption, which is beneficial to improve the performance of solar cells. Finally, by adopting the best inverted pyramid texture, the corresponding mono-crystalline silicon PERC solar cell obtained a high efficiency of 22.69% with V_{oc} of 680.42 mV, J_{sc} of 41.20 mA/cm^2 , FF of

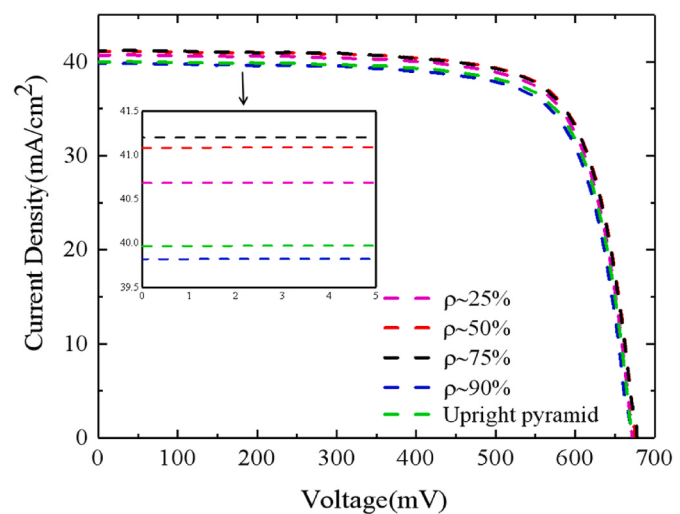


Fig. 13. The I–V curves of mono-crystalline silicon PERC solar cells fabricated by different ρ values.

Table 4

The electrical performance of the solar cells with different ρ values.

Sample	Eff (%)	J_{sc} (mA/ cm^2)	V_{oc} (mV)	FF (%)	Calculate J_{sc} (mA/ cm^2)
$\rho \sim 25\%$	22.03	40.73	672.95	80.38	39.666
$\rho \sim 50\%$	22.42	41.13	676.76	80.54	39.961
$\rho \sim 75\%$	22.69	41.20	680.42	80.94	40.115
$\rho \sim 90\%$	21.41	39.82	670.09	80.23	38.776
Upright pyramid	21.58	39.97	672.22	80.32	38.878

80.94% for large area of $156.75 \times 156.75 \text{ mm}^2$ wafer respectively. In summary, the texture structure and reflectivity performance of mono-crystalline silicon solar cell can be optimized by adjusting ρ value, and the suitable ρ value can improve solar cell performance. The achievement of high performance mono-crystalline silicon PERC solar cell indicates the uniform inverted pyramid texture has great potential to fabricate high efficiency PERC solar cells in large-scale production.

Credit authorship contribution statement

Danni Zhang: Validation, Data curation, Formal analysis, Investigation, Simulated Data, Writing – original draft, Writing – review & editing. **Longjie Wang:** Validation, Data curation. **Rui Jia:** Methodology, Data curation, Writing – original draft, Writing – review & editing, Project administration. **Ke Tao:** Conceptualization, Data curation, Writing – review & editing, Project administration. **Shuai Jiang:** Investigation. **Huayun Ge:** Investigation. **Bolong Wang:** Validation. **Zhibo Gao:** Investigation. **Xinpu Li:** Investigation. **Minghui Li:** Investigation. **Zhi Jin:** Investigation.

Declaration of competing interest

The authors declare that they have no known competing financial interests or personal relationships that could have appeared to influence the work reported in this paper.

Acknowledgements

This work was supported by the National Key Research and Development Program of China (2018YFB1500500, 2018YFB1500200, 2020YFB1506503), National Natural Science Foundation of China (NSFC, Grant Nos. 12035020, 52072399, 62074165), Natural

Science Foundation of Beijing Municipality (4192064,1212015) and JKW Project 31512060106.

References

- [1] K.R. Catchpole, A.W. Blakers, Modelling the PERC structure for industrial quality silicon, *Sol. Energy Mater. Sol. Cells* 73 (2002) 189–202.
- [2] C. H Hsu, J.R. Wu, Y.T. Lu, et al., Fabrication and characteristics of black silicon for solar cell applications: an overview, *Mater. Sci. Semicond. Process.* 25 (2014) 2–17.
- [3] H. Gong, M. Li, L. Zhou, A study of mottling phenomenon on textured multicrystalline silicon wafers and its potential effects on solar cell performance, *Mater. Sci. Semicond. Process.* 26 (2014) 149–154.
- [4] K. Gao, Y. Liu, Y. Fan, L. Shi, High-efficiency silicon inverted pyramid-based passivated emitter and rear cells, *Nanoscale Research Lett* 15 (174) (2020) 2–9.
- [5] M. Ju, K. Mallen, S. Dutta, N. Balaji, Influence of small size pyramid texturing on contact shading loss and performance analysis of Ag-screen printed mono crystalline silicon solar cells, *Mater. Sci. Semicond. Process.* 85 (2018) 68–75.
- [6] L. Yang, Y. Liu, Y. Wang, W. Chen, 18.87%-efficient inverted pyramid structured silicon solar cell by one-step Cu-assisted texturization technique, *Sol. Energy Mater. Sol. Cells* 166 (2017) 121–126.
- [7] Q. Tang, H. Shen, H. Yao, K. Gao, Cu-assisted chemical etching of bulk c-Si: a rapid and novel method to obtain 45 μm ultrathin flexible c-Si solar cells with asymmetric front and back light trapping structures, *Sol. Energy* 170 (2018) 263–272.
- [8] C. Zhang, L. Chen, Y. Zhu, Z. Guan, Fabrication of 20.19% efficient single-crystalline silicon solar cell with inverted pyramid microstructure, *Nanoscale Research Lett* 13 (2018).
- [9] Y. Jiang, H. Shen, T. Pu, C. Zheng, High efficiency multi-crystalline silicon solar cell with inverted pyramid nanostructure, *Sol. Energy* 142 (2017) 91–96.
- [10] A.P. Amalathas, M.M. Alkaisi, Efficient light trapping nanoparamid structures for solar cells patterned using UV nanoimprint lithography, *Mater. Sci. Semicond. Process.* 57 (2017) 54–58.
- [11] A. Stafp, F. Honeit, C. Gondek, E. Kroke, Texturing of monocrystalline silicon wafers by HF-HCl-H₂O₂ mixtures: generation of random inverted pyramids and simulation of light trapping in PERC solar cells, *Sol. Energy Mater. Sol. Cells* 159 (2017) 112–120.
- [12] D.N. Zhang, S. Jiang, K. Tao, Fabrication of inverted pyramid structure for high-efficiency silicon solar cells using metal assisted chemical etching method with CuSO₄ etchant, *Sol. Energy Mater. Sol. Cells* 230 (2021) 111200.
- [13] J.S. Yoo, I.O. Parm, U. Gangopadhyay, K. Kim, Black silicon layer formation for application in solar cells, *Sol. Energy Mater. Sol. Cells* 90 (2006) 3085–3093.
- [14] S. Sivasubramaniam, M.M. Alkaisi, Inverted nanoparamid texturing for silicon solar cells using interference lithography, *Microelectron. Eng.* 119 (2014) 146–150.
- [15] K. Kumar, K.C. Lee, J. Nogami, et al., Ultrafast laser direct hard-mask writing for high performance inverted-pyramidal texturing of silicon, in: 2012 38th IEEE Photovoltaic Specialists Conference (PVSC). IEEE, 2012.
- [16] T. Pu, H. Shen, C. Zheng, Y. Xu, Temperature effect of nano-structure rebuilding on removal of DWS mc-Si marks by Ag/Cu MACE process and solar cell, *Energies* 13 (2020) 4890.
- [17] Y. Zhao, Y. Liu, W. Chen, J. Wu, Regulation of surface texturization through copper-assisted chemical etching for silicon solar cells, *Sol. Energy* 201 (2020) 461–468.
- [18] K. Peng, Y. Wu, H. Fang, Uniform axial-orientation alignment of one-dimensional single-crystal silicon nanostructure arrays, *Angew. Chem.* 117 (2005) 2797–2802.
- [19] K.Q. Peng, J.J. Hu, Y.J. Yan, Fabrication of single-crystalline silicon nanowires by scratching a silicon surface with catalytic metal particles, *Adv. Funct. Mater.* 16 (2006) 387–394.
- [20] P. Zhang, R. Jia, K. Tao, S. Jiang, The influence of Ag-ion concentration on the performance of mc-Si silicon solar cells textured by metal assisted chemical etching (MACE) method, *Sol. Energy Mater. Sol. Cells* 200 (2019) 109983.
- [21] X. Li, K. Tao, D. Zhang, Z. Gao, R. Jia, Development of additive-assisted Ag-MACE for multicrystalline black Si solar cells, *Electrochim. Commun.* 113 (2020) 106686.
- [22] C.H. Hsu, J.R. Wu, Y.T. Lu, D.J. Flood, Fabrication and characteristics of black silicon for solar cell applications: an overview, *Mater. Sci. Semicond. Process.* 25 (2014) 2–17.
- [23] K. Gao, H. Shen, Y. Liu, Y. Jiang, Enhanced etching rate of black silicon by Cu/Ni Co-assisted chemical etching process, *Mater. Sci. Semicond. Process.* 88 (2018) 250–255.
- [24] N. Mitsugi, K. Nagai, Pit formation induced by copper contamination on silicon surface immersed in dilute hydrofluoric acid solution, *Journal of the electrochemical soc* 151 (2004) G302.
- [25] H. Zheng, M. Han, P. Zheng, L. Zheng, Porous silicon templates prepared by Cu-assisted chemical etching, *Marter. Lett.* 118 (2014) 146–149.
- [26] Q. Tang, H. Yao, B. Xu, J. Ge, Enhanced energy conversion efficiency of Al-BSF c-Si solar cell by a novel hierarchical structure composed of inverted pyramids with different sizes, *Sol. Energy* 208 (2020) 1–9.
- [27] J.R. Meyer-Arendt, J.W. Blaker, Introduction to classical and modern optics, *American journal of phy* 41 (1973) 148–149.
- [28] K.W.A. Chee, Z. Tang, H. Lü, F. Huang, Anti-reflective structures for photovoltaics: numerical and experimental design, *Energy Rep.* 4 (2018) 266–273.
- [29] F. Zhao, X. Chen, Z. Yi, F. Qin, Study on the solar energy absorption of hybrid solar cells with trapezoid-pyramidal structure based PEDOT:PSS/c-Ge, *Sol. Energy* 204 (2020) 635–643.
- [30] X. Li, K. Tao, H. Ge, D. Zhang, Improvement of saw damage removal to fabricate uniform black silicon nanostructure on large-area multi-crystalline silicon wafers, *Sol. Energy* 204 (2020) 577–584.
- [31] G. Scardera, S.Z. Wang, Y. Zhang, On the enhanced phosphorus doping of nanotextured black silicon, *IEEE Journal of Photovoltaics* 11 (2021) 298–305.
- [32] Y. Li, Q. Chen, B. Wu, Broadband perfect metamaterial absorber based on the gallium arsenide grating complex structure, *Results in Physics* 15 (2019) 102760.
- [33] J Oh, H Yuan, H.M Branz, An 18.2%-efficient black-silicon solar cell achieved through control of carrier recombination in nanostructures, *Nature Nanotechnol.* 7 (2012) 743–748.